J Mater Sci (2011) 46:6941–6951
DOI 10.1007/s10853-011-5660-z

Optimization of composition and heat treatment design of Mg–Sn–Zn alloys via the CALPHAD method

S. Avraham · A. Katsman · M. Bamberger

Received: 29 January 2011 / Accepted: 24 May 2011 / Published online: 4 June 2011

Abstract This work is focused on the application of the calculation of phase diagrams method for alloy and heat treatment design. We analyzed the influence of Zn content on the precipitation of Mg_2Sn in Mg–Sn–Zn alloys. A comparison with previous studies in the Mg–Sn–Zn system was made according to the published results and computational thermochemistry simulations. The phase evolution in the Mg–Sn–Zn system was evaluated for the different compositions, and the simulations were used for precise alloy and heat treatment design. The composition of the ternary alloy was set as Mg–8wt%Sn–1.25wt%Zn. The Sn and Zn content was designed and confirmed to be within the α-Mg solubility limit at the solution treatment temperature. The addition of Zn and the heat treatment applied resulted in the enhancement and refinement of the Mg_2Sn precipitation. Three Vickers micro-hardness maxima were detected: precipitation of metastable Mg–Zn phases, heterogeneous precipitation of Mg_2Sn on the Mg–Zn precipitates, and Mg_2Sn precipitation in the α-Mg matrix. The CT simulations were found to be a valuable alloy design tool.

Introduction

Mg alloys are highly attractive for engineering applications due to their high specific mechanical properties [1–3]. The high-temperature properties of an alloy can be improved by the precipitation of intermetallics with high-temperature stability. The intermetallics distributed inside the grains can pin dislocations during creep [4].

S. Avraham · A. Katsman · M. Bamberger (✉)
Department of Materials Engineering, Technion-Israel Institute of Technology, 32000 Haifa, Israel
e-mail: mtrbam@tx.technion.ac.il

The development of a new alloy is determined by the alloy composition, alloy constituents, and processing parameters. Alloy development experiments are time- and resource-consuming. Computational thermochemistry (CT), based on the calculation of phase diagrams method (CALPHAD) method, can be utilized in the development of alloys or optimization of material-dependent processes [5]. The equilibrium state of a multi-component alloy is derived by minimizing the total Gibbs energy at constant temperature, pressure, and composition. This method is successfully applied in the development of Mg alloys [6, 7].

The Mg–Sn system is age-hardenable, with the maximum solubility limit of Sn in α-Mg being $\sim$14.67 wt% at $T \cong 560$ °C (all composition-related units will be in wt% hereafter) [4, 8]. Mg_2Sn is a high-melting temperature phase ($T_m \approx 770$ °C) that can form in significant amounts via precipitation hardening [8].

Mg–Zn precipitation-hardenable alloys are commonly used Mg alloys, with the Zn addition, among others, improving room-temperature properties [4, 9]. The maximum solubility of Zn in α-Mg is 6.2 wt% at $T \cong 340$ °C [8]. Controlled decomposition of the Mg–Zn solid solution results in an age-hardening effect. Mg_4Zn_7 has been detected as the metastable phase, $MgZn_2$ as the intermediate phase, and MgZn as the most stable phase [10, 11].

Mendis et al. [12] and Sasaki et al. [13] analyzed the effect of the addition of Zn to Mg–Sn alloys (Mg–6.04Sn–*x* Zn and Mg–9.9Sn–*x*Zn, respectively). They found [12, 13] that the presence of Zn in Mg–Sn–Zn alloys: (i) refines the Mg_2Sn precipitates (2–1 μm → 0.5–1 μm), (ii) makes the Mg_2Sn precipitation more homogenous, (iii) increases the number density of plate-like precipitates and rod-shaped precipitates lying on non-basal (prismatic and pyramidal) planes, and (iv) reduces the time to Vickers micro hardness (VMH) peak from 8×10^6 to 5×10^6 s. It was suggested

that Zn alters the interfacial energy between Mg_2Sn and α-Mg, which leads to the increased number of rod- and plate-shaped precipitates in the Zn-containing alloys [12, 13].

Cohen et al. [11] investigated the aging response of Mg–3.8Sn–4.5Zn at 175 °C over a 4-day period. Two VMH peaks were detected, at about 7.2×10^3 s and at about 5.76×10^4 s. X-ray diffraction (XRD) and transmission electron microscopy (TEM) analysis revealed that the first peak can be correlated to the precipitation of the $MgZn_2$ phase, whereas the second was correlated to the precipitation of the Mg_2Sn phase. This was confirmed by small-angle X-ray scattering and TEM results [14]. These findings are consistent with the analysis performed on Mg–5.6Sn–4.41Zn–2.1Al and Mg–3.98Sn–4.41Zn–0.62Y alloys [15, 16]. Meng et al. [17] optimized the Mg–Sn, Mg–Zn and Sn–Zn binary systems, and the thermodynamic modeling of the Mg–Sn–Zn ternary system was presented.

This work is focused on analyzing the effect of Zn content variation in the Mg–Sn–Zn ternary system. The analysis is performed based on the present and previously published results, and the appropriate CT simulations.

Calculation

CT simulation method

The formation of different phases during solidification was predicted using the software developed by Thermo-Calc AB of Stockholm, Sweden [18, 19]. The simulation results were based on thermodynamic considerations and a specially developed database [5, 17]. The principles of the CALPHAD methodology were detailed by Saunders et al. [5] and in the Thermo-Calc manual [19].

Solidification (casting), in practice, does not proceed under thermodynamic equilibrium. In the course of solidification, the liquid is enriched with alloying elements and non-equilibrium phases form [20]. Therefore, equilibrium solidification and non-equilibrium solidification (based on the Scheil–Gulliver model [20–22]) are simulated to predict the solidification process, precipitation sequence (phases, relevant temperatures, etc.), and the weight fraction of the different phases during and after solidification.

Alloy composition selection, phase stability, and heat treatment design

To analyze the effect of varying the Zn content in a magnesium alloy containing Sn at a predetermined amount, an isopleth presentation was used. Figure 1 presents a CT-based equilibrium T–C section for (a) Mg–6.04Sn–*x*Zn, (b) Mg–8Sn–*x*Zn, and (c) Mg–9.9Sn–*x*Zn alloys with varying Zn content ($0 \le x \le 6$ wt%). The Mg–6.04Sn–*x*Zn and Mg–9.9Sn–*x*Zn alloys were based on the composition derived by Mendis et al. [12] and Sasaki et al. [13], respectively. One can observe that the increase in the Sn content resulted in two significant effects: the decreases of the single α-Mg phase region, and an increase of the three-phase liquid + α-Mg + Mg_2Sn region.

The increase in the Sn content in the alloys (Mg–6.04Sn–*x*Zn, Mg–8Sn–*x*Zn, and Mg–9.9Sn–*x*Zn) resulted in a combined effect: a slight shift in the equilibrium transition between the two-phase liquid + α-Mg region and the single α-Mg region to lower temperatures, and a shift in the equilibrium transition between the single α-Mg region and the two-phase α-Mg + Mg_2Sn region to higher temperatures. As a result of the Sn content increase the single α-Mg phase temperature stability range and maximal Zn content (allowing a α-Mg single-phase region) decreases.

The maximum solubility limit of Zn in the single-phase α-Mg decreased from 5.3 wt% at 366 °C (Mg–6.04Sn–*x*Zn; Fig. 1a) to 4.1 wt% at 414 °C (Mg–8Sn–*x*Zn; Fig. 1b) and 3 wt% at 458 °C (Mg–9.9Sn–*x*Zn; Fig. 1c). In the

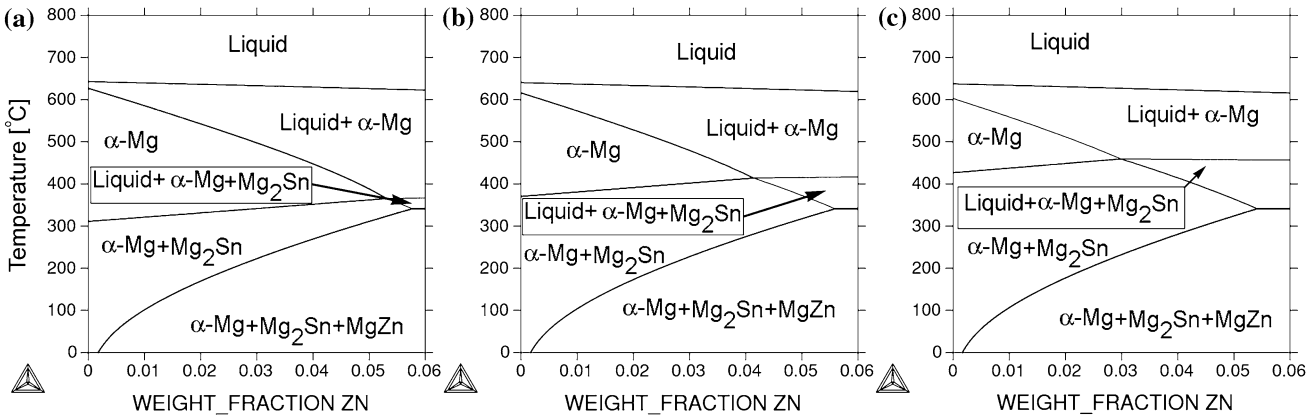

Fig. 1 CT-based equilibrium T–C section for **a** Mg–6.04Sn–*x*Zn, **b** Mg–8Sn–*x*Zn, and **c** Mg–9.9Sn–*x*Zn alloys with varying Zn content ($0 \le x \le 6$ wt%). The Mg–6.04Sn–*x*Zn and Mg–9.9Sn–*x*Zn simulations were conducted to assess the available results [12, 13]

Mg–8Sn–1.25Zn alloy, the Zn content (1.25 wt%) was set to be within the α-Mg solubility limit at the solution treatment temperature. An excess Zn amount in the alloy can result in the presence of a liquid phase during the solution stage, incomplete dissolution in the α-Mg matrix, and an inferior age-hardening response.

The transition line between the single-phase α-Mg region to the two-phase α-Mg + Mg_2Sn region rises from 311–366 °C (Mg–6.04Sn–*x*Zn; Fig. 1a) to 371–414 °C (Mg–8Sn–*x*Zn; Fig. 1b) and 427–458 °C (Mg–9.9Sn–*x*Zn; Fig. 1c). The transition line between the two-phase α-Mg + Mg_2Sn region to the triple-phase α-Mg + Mg_2Sn + MgZn region appears to be independent of the Sn composition variation. The T–C section should be considered while selecting the Mg–Sn–Zn composition and determining the heat treatment parameters for optimal precipitation-hardening response in the solid state.

Two alloys were derived in the present work: Mg–8Sn and Mg–8Sn–1.25Zn. The selection of the Sn content in the alloys was motivated by the presence of a single-phase α-Mg region for heat treatment (a composition that allows a low solution treatment temperature) and maximum solubility of the alloying elements in α-Mg [8]. The Sn content was compromised at 8% according to: (i) the maximum solubility limit of Sn in α-Mg ($\sim$14.48 wt% at $T \cong 560$ °C) and (ii) the transition temperature ($T \cong 460$ °C) between the α-Mg single phase region to the α-Mg + Mg_2Sn two-phase region [4, 8]. The transition temperature from the single- to the two-phase region determines the minimum temperature allowed for the solution treatment. The solution treatment temperature (520 °C) was selected: (i) in a single-phase region with complete solubility of the alloying elements (according to the equilibrium CT results for both alloys), and (ii) to allow fast diffusion of Sn in the α-Mg matrix during the solution treatment.

The dwell time at the solution temperature was derived $\left(t \cong d^2/\left(D_{\mathrm{Sn}}(\mathrm{Mg})\right)\right)$ according to the average grain size radius, d, and the diffusion coefficients of Sn in α-Mg, $D_{\mathrm{Sn}}(\mathrm{Mg})$. It should be noted that the diffusion coefficient of Sn in α-Mg is smaller than that of Zn. At the 100–520 °C temperature range, the ratio $D_{\mathrm{Sn}}(\mathrm{Mg})/D_{\mathrm{Zn}}(\mathrm{Mg})$ varies between $\sim 6 \times 10^{-4}$ and ~ 0.1, respectively [23].

Materials and methods

Alloy preparation and heat treatment procedure

The samples ($\sim$220 g) were produced by the melting of pure α-Mg (Dead Sea Magnesium, >99.9 at.%), Sn (SPECTRUM, T1065, >99.5 at.%), and Zn (SPECTRUM, Z1035, >99.8 at.%) in a cemented carbide crucible. The melting was conducted under protective atmosphere (CO_2 + Freon 134) at $T = 750$ °C and casting in a steel mold. The composition of the alloys was analyzed and confirmed by inductively coupled plasma optical emission (ICP-OE) performed by DIRATS Laboratories, Westfield, MA, USA, with the use of a Perkin-Elmer Optima 3300 DV.

The as-cast samples were encapsulated in sealed quartz tubes filled with low-pressure Ar gas. The solution treatment for the Mg–8Sn alloy was designed as follows: heating of the as-cast samples (50 °C/h) to the solution treatment temperature (520 °C), a 22-h dwell at the same temperature, and water quenching to RT. According to the non-equilibrium CT simulations, no eutectic solidification is expected below 570 °C; thus, rapid heating (50 °C/h) and solution treatment at 520 °C are applicable.

According to the non-equilibrium CT simulations (will be presented) and experimental results related to the Mg-rich section of the Mg–Zn phase diagram [8] eutectic solidification is expected for the Mg–8Sn–1.25Zn alloy at 340 °C. As a result, the Mg–8Sn solution treatment was modified; a 96-h dwell at 320 °C allows the dissolution of the eutectic structure and homogenous distribution of the alloying elements. This is followed with quasi-static heating (10 °C/h) to prevent possible melting of any residual eutectic structure at the GB. The Mg–8Sn–1.25Zn alloy was solution treated at 520 °C for 22-h, this was followed with water quenching to RT.

The aging of the supersaturated solid solution samples was conducted by suspending the samples in a stirred molten (175 °C) salt (sodium nitrate 50 wt% + potassium nitrate 50 wt%) bath. The maximum aging time was 32 days. All time units related to aged samples will be in seconds hereafter.

Differential scanning calorimetry

The purpose of the differential scanning calorimetry (DSC) analysis was to measure the characteristic temperatures (peak and onset temperatures) of the phase transitions. The DSC analysis was performed by using a Setaram Labsys™ DSC system (S-type thermocouple, PtRh 10%Pt, RT 1500 °C) [24]. The sample ($\sim$30 mg) was analyzed in a graphite crucible under a dynamic Ar atmosphere (99.999%) (gas flow rate: 25 mL/min). Temperature and heat flow calibrations were performed with the use of pure calibration elements (In, Sn, Pb, Zn, Al, and Ag) with heating rates of 2, 5, and 10 °C/min.

Microstructural stability tests and microstructure characterization

VMH measurements were conducted to track the thermal stability of the alloys during prolonged aging at 175 °C. The samples for VMH measurements were sliced (10·10·5[mm]) and cold-mounted in an epoxy resin. The sample was polished on a series of SiC polishing paper, with a final polishing step using an Al_2O_3 particle (0.05 μm, Buehler) suspension in water. The VMH measurements were conducted using a DMH-2 micro-hardness tester (MATSUZAWA SEIKS CO. LTD Japan). The load level was set to 50 grf and the load time to 15 s. The VMH of each sample was determined as the average of a minimum of 20 individual indentations.

XRD, utilizing a Philips PW-3020 X-ray automatic powder diffractometer in Bragg–Brentano geometry with a Cu Kα radiation tube operating at 40 mA and 40 kV (Philips, PW-1820), was used for phase identification. The XRD samples were polished using the same method as the VMH samples. XRD 2θ scans were acquired in the range of 10° to 100°, with a step size of 0.02° and an exposure time of 9 s per step. The XRD results were analyzed with the DDView + 4 software, and the crystallographic nature of the phases was identified according to the PDF-4 + 2008 database [25].

Scanning electron microscopy (SEM) was conducted to evaluate the microstructure of the different alloys, the different phases that are present and the influence of the thermal treatments on the microstructure evolution. The VMH samples were used for SEM analysis, they were polished using the same procedure. The composition of the different phases was be evaluated by energy dispersive spectroscopy (EDS). SEM was conducted using a FEI Quanta 200 [26]. Secondary electron (SE) and back-scattered electron (BSE) were used for imaging. This instrument is equipped with an EDS system (INCA 350, Oxford Instruments, UK) for elemental microanalysis of the sample. The accelerating voltage during the analysis was 20 kV and the working distance was 10.5 mm.

Results

CT simulations—high Sn composition: phase stability, DSC, and heat treatment design

CT simulations of the equilibrium and the non-equilibrium phase evolution in the Mg–8Sn (a) and Mg–8Sn–1.25Zn (b) alloys are presented in Figs. 2 and 3, respectively. During equilibrium solidification of the Mg–8Sn alloy (Fig. 2a), α-Mg starts to solidify at the liquidus temperature T_L (641 °C); DSC results set the T_L temperature at 635 °C. According to the equilibrium solidification simulations, solidification is terminated at 616 °C. The supersaturation of α-Mg with Sn in the Mg–8Sn alloy initiates the formation of Mg_2Sn at ~371 °C. The α-Mg single-phase region therefore exists between 616 and 371 °C.

The non-equilibrium CT simulation for Mg–8Sn (see Fig. 3a), according to the Scheil–Gulliver model, shows that below ~640 °C α-Mg forms, and its weight fraction rapidly increases with the decrease in temperature. Eutectic solidification takes place above ~561 °C when α-Mg and Mg_2Sn form; at this stage the liquid is consumed, and the non-equilibrium CT simulation is terminated. The eutectic temperature (T_{eut}) for the Mg–8Sn alloy is in good agreement with the T_{eut} measured by DSC (~553 °C) and with T_{eut} for the Mg-rich part (~560 °C) of the Mg–Sn binary system [8].

Figure 2b presents the results of the CT simulation of the equilibrium phase evolution during cooling of the Mg–8Sn–1.25Zn alloy. α-Mg starts to solidify at T_L (~633 °C), with DSC results (Fig. 4) setting T_L at ~625 °C. Solidification terminates at ~562 °C. Mg_2Sn starts to precipitate at 383 °C, and formation of MgZn is expected below ~121 °C. The α-Mg single-phase region exists between 562 and 383 °C.

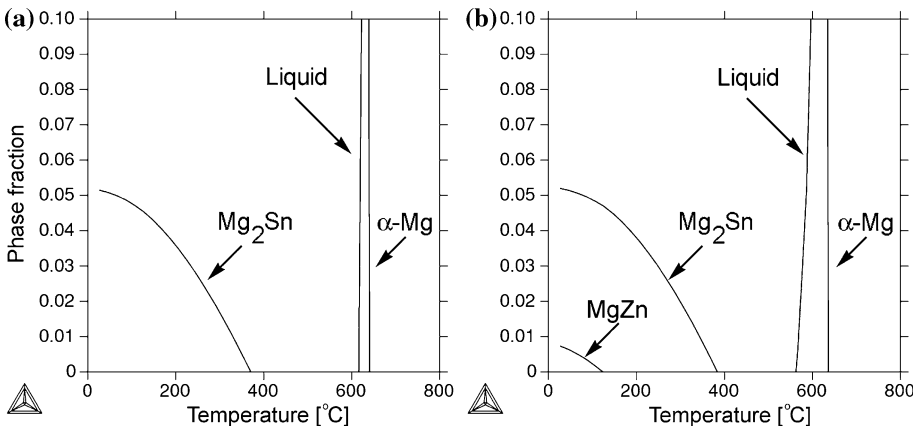

Fig. 2 The equilibrium phase evolution CT simulations for **a** Mg–8Sn and **b** Mg–8Sn–1.25Zn alloys

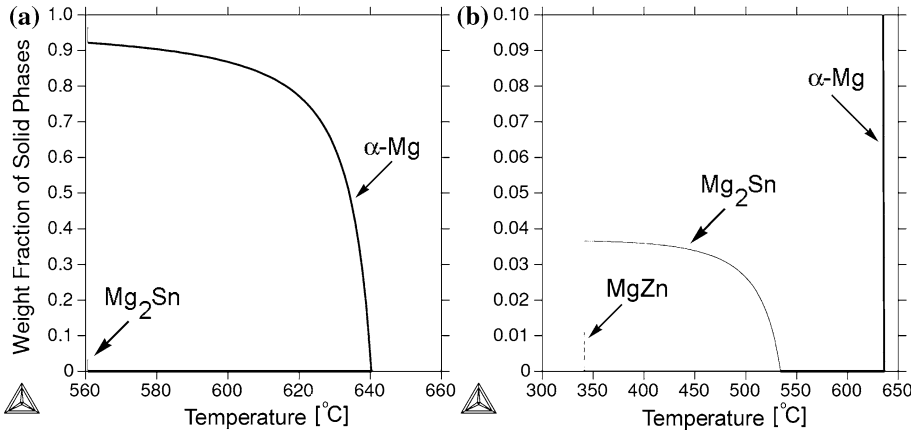

Fig. 3 The non-equilibrium phase evolution CT simulations for **a** Mg–8Sn and **b** Mg–8Sn–1.25Zn alloys

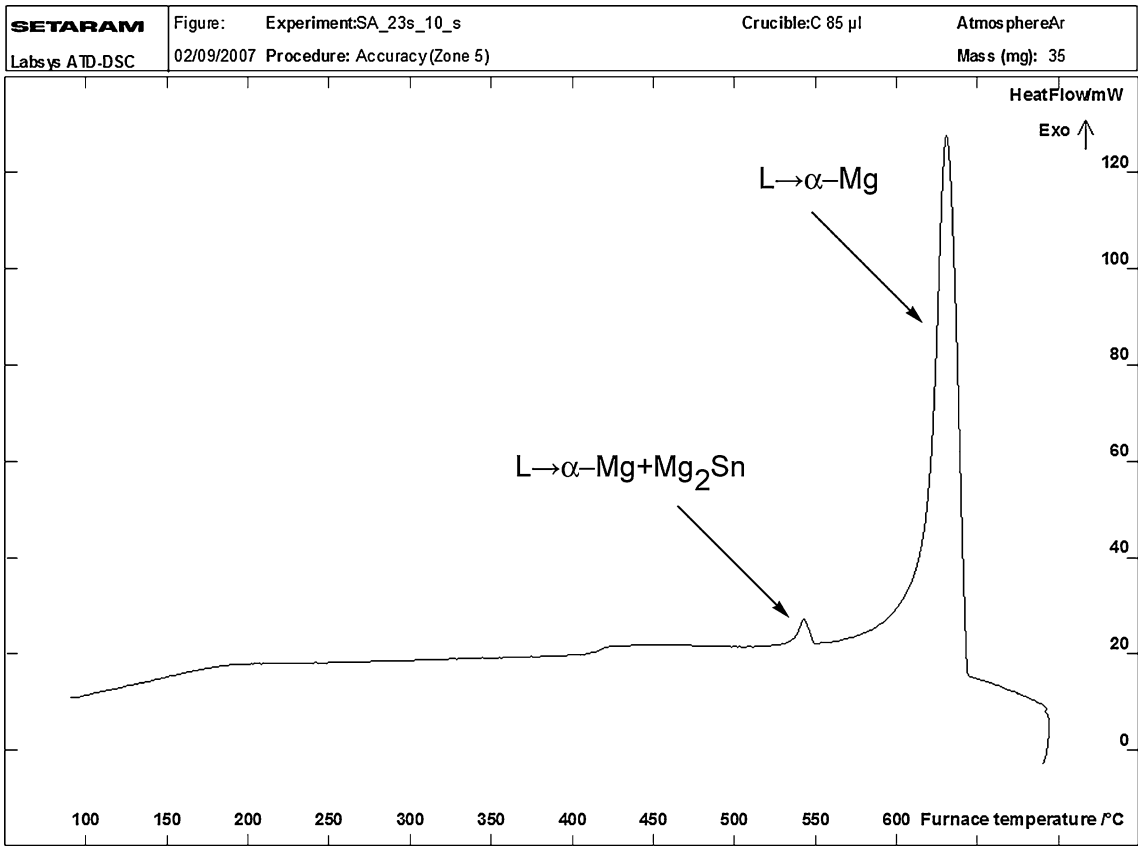

Fig. 4 DSC analysis results measured during cooling (10 °C/min) for the Mg–8Sn–1.25Zn alloy

The non-equilibrium CT simulation for the Mg–8Sn–1.25Zn alloy (see Fig. 3b) shows that below ~636 °C α-Mg forms. Mg_2Sn forms during an eutectic reaction below ~534 °C, DSC results (Fig. 4) set T_{eut} at ~530 °C. Solidification is terminated by the invariant reaction ($L + Mg_2Sn \leftrightarrow$ α-Mg + MgZn [17]) at the invariant temperature (T_{inv}) of ~341 °C.

The equilibrium phase evolution CT simulations performed for the compositions of the Mg–6.04Sn–*x*Zn [12] and Mg–9.9Sn–*x*Zn [13] alloys are presented in Figs. 5 and 6, respectively. Table 1 summarizes the CT simulation results for the equilibrium and non-equilibrium phase evolution of the Mg–6.04Sn–*x*Zn, Mg–8Sn–*x*Zn, and Mg–9.9Sn–*x*Zn alloys.

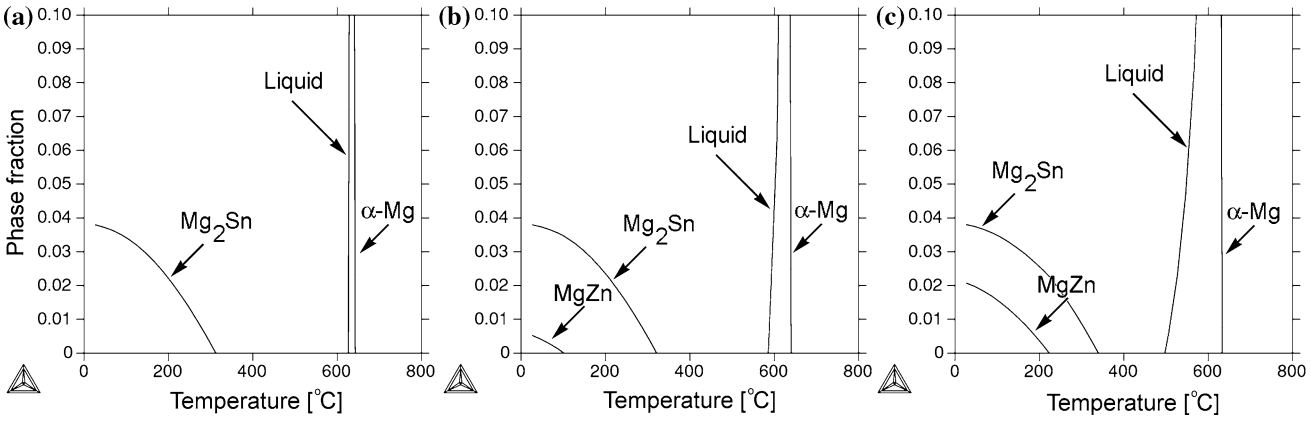

Fig. 5 The equilibrium phase evolution CT simulations performed for **a** Mg–6.04Sn, **b** Mg–6Sn–1Zn, and **c** Mg–5.93Sn–3.01Zn alloys. The CT simulations were conducted to assess the available results [12]

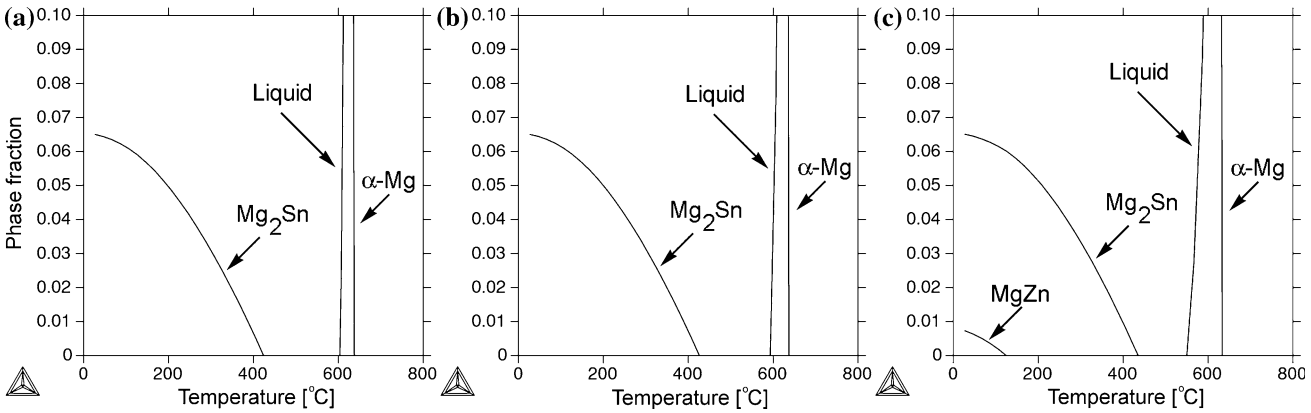

Fig. 6 The equilibrium phase evolution CT simulations performed for **a** Mg–9.9Sn, **b** Mg–9.88Sn–0.25Zn, and **c** Mg–9.82Sn–1.23Zn alloys. The CT simulations were conducted to assess the available results [13]

The increase in the Sn content of the Mg–Sn binary alloys results in a decrease in the α-Mg single-phase region width from 315 °C (Mg–6.04Sn) to 245 °C (Mg–8Sn) and 181 °C (Mg–9.9Sn). In addition, an increase in the initial temperature at which Mg_2Sn forms ($T_{init}^{Mg_2Sn}$) is observed. The increase in the Zn content of each of the alloys decreases the α-Mg single-phase region width, increases the initial temperature at which Mg_2Sn $\left(T_{init}^{Mg_2Sn}\right)$ and MgZn forms $\left(T_{init}^{MgZn}\right)$.

The addition of Zn to each of the binary alloys decreases the T_{inv} in a significant manner ($\sim$560 °C $\rightarrow$ $\sim$340 °C). A comparison of the alloys with similar Zn content (1–1.25 wt%) and increasing Sn content shows that the α-Mg single-phase region width decreases, and $T_{init}^{Mg_2Sn}$ increase. The T_{init}^{MgZn} and T_{inv} appear to be independent of the Sn content. One should note that excessive Zn content can result in a narrow α-Mg single-phase region or its absence (Fig. 1).

Table 1 The CT simulation results for the equilibrium and non-equilibrium phase evolution of the Mg–6.04Sn–*x*Zn, Mg–8Sn–*x*Zn, and Mg–9.9Sn–*x*Zn alloys

Alloy	Temperature range for single α-Mg phase	$T_{init}^{Mg_2Sn}$ (°C)	T_{init}^{MgZn} (°C)	T_{inv} (°C)
Mg–6.04Sn	315	312	–	561
Mg–6Sn–1Zn	265	320	98	342
Mg–5.93Sn–3.01Zn	160	338	222	342
Mg–8Sn	245	371	–	561
Mg–8Sn–1.25Zn	179	383	121	341
Mg–9.9Sn	181	423	–	561
Mg–9.88Sn–0.25Zn	167	426	–	341
Mg–9.82Sn–1.23Zn	117	433	123	341

CT simulations—low Sn composition: alloy composition selection, phase stability, and heat treatment design

The experimental results relating to Mg–Sn–Zn alloys with low Sn content can contribute to the understanding of the

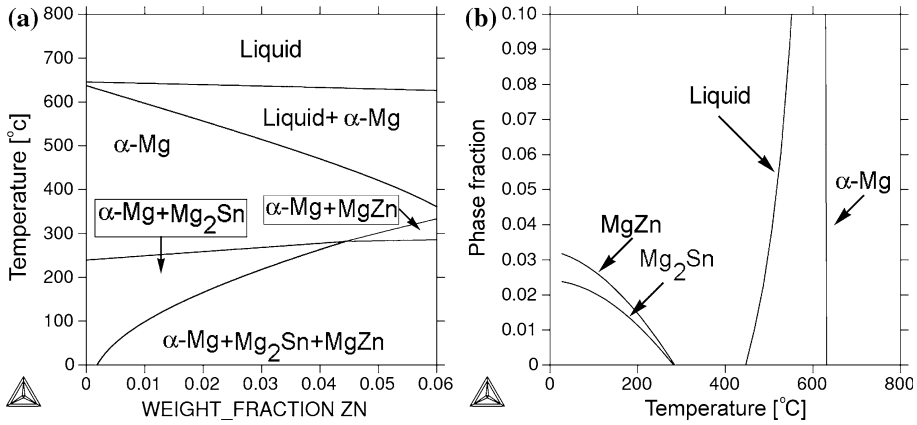

Fig. 7 Equilibrium CT-based **a** T–C section of the Mg–3.8Sn–*x*Zn alloy with varying Zn content and **b** phase evolution during equilibrium cooling of the Mg–3.8Sn–4.5Zn alloy. The Mg–3.8Sn–*x*Zn simulations were conducted to assess the available results [11, 14]

Mg–Sn–Zn system. The equilibrium CT-based T–C section for the Mg–3.8Sn–*x*Zn alloy with varying Zn content [11, 14] is presented in Fig. 7a; the CT simulations were conducted in order to assess the available results. The width of the α-Mg single-phase region is rather large. The transition line between the single α-Mg region and the two-phase α-Mg + Mg_2Sn region ranges between 239 and 281 °C. For Mg–3.8Sn–*x*Zn alloys with a Zn content higher than 4.45 wt%, the MgZn phase forms from the saturated α-Mg phase at high temperatures preceding the Mg_2Sn phase formation.

Figure 7b presents the phase evolution during equilibrium cooling of the Mg–3.8Sn–4.5Zn alloy. The solidification of α-Mg starts at T_L (~631 °C) and terminates at ~447 °C. MgZn and Mg_2Sn start to precipitate at 282 °C. The phase weight fraction of MgZn is higher than that of Mg_2Sn, a result of the high Zn content with respect to Sn. The non-equilibrium CT simulation, according to the Scheil–Gulliver model, shows that the eutectic temperature for the Mg–3.8Sn–4.5Zn alloy is ~341 °C. The T_{inv} for the Mg–3.8Sn–4.5Zn alloy is in good agreement with the T_{eut} (~340 °C) for the Mg-rich part of the Mg–Zn binary system [8].

Microstructural stability tests and analysis

Figure 8 presents the VMH results of the Mg–8Sn and Mg–8Sn–1.25Zn alloys during aging (175 °C, $t \leq 2.76 \times 10^6$ s). The Mg–9.9Sn–*x*Zn VMH results of Sasaki et al. [13] are added for comparison purposes.

The initial VMH of the Mg–8Sn–1.25Zn alloy was ~62 [HV]. Three maxima, VMH-I, VMH-II, and VMH-III (~65, ~74, and 79 [HV], respectively), were observed after ~3.6×10^3–4.32×10^4, ~1.01×10^5, and ~6.9×10^5–2.76×10^6 s, respectively. The initial VMH of the Mg–8Sn alloy was ~53 [HV]; after 3.6×10^3 s it equalized the VMH of the aged Mg–8Sn–1.25Zn alloy. Two maxima, VMH-II and VMH-III (~65 and 69 [HV],

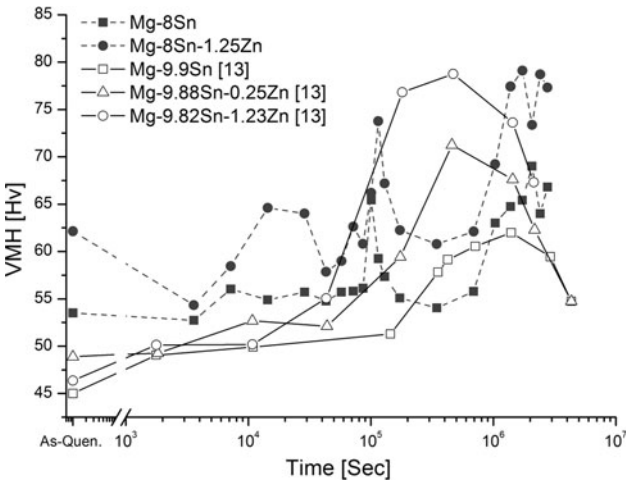

Fig. 8 VMH results of the Mg–8Sn and Mg–8Sn–1.25Zn alloys during aging ($T = 175$ °C, $t \leq 2.76 \times 10^6$ s); the results of Sasaki et al. [13] are presented for comparison purposes

respectively), could be observed at ~1×10^5 and ~1.72×10^6 s, respectively.

It appears that the addition of Zn to the Mg–8Sn alloy resulted in increased solid solution strengthening after quenching to RT, the formation of an early maximum (VMH-I) at ~3.6×10^3–4.32×10^4 s, and the enhancement of the two (VMH-II and VMH-III) maxima. It should be noted that in the work of Sasaki et al. [13], the increased Zn content in the Mg–9.9Sn alloy resulted in the enhancement of a single VMH peak (VMH-III); the onset time was reduced, but the first two VMH peaks observed during our work were not resolved (see Fig. 8).

Figure 9 presents the XRD pattern of the (a) Mg–8Sn and (b) Mg–8Sn–1.25Zn alloys during aging (175 °C, $t = 1.73 \times 10^5$ s, VMH-II). As it can be seen the presence of Mg_2Sn was detected in the Mg–8Sn–1.25Zn alloy, Mg_2Sn was not detected by XRD in the aged Mg–8Sn alloy. The presence of Zn in the Mg–8Sn–1.25Zn alloy enhances the precipitation of Mg_2Sn after $t = 1.73 \times 10^5$ s. Table 2 summarizes the phases detected by XRD

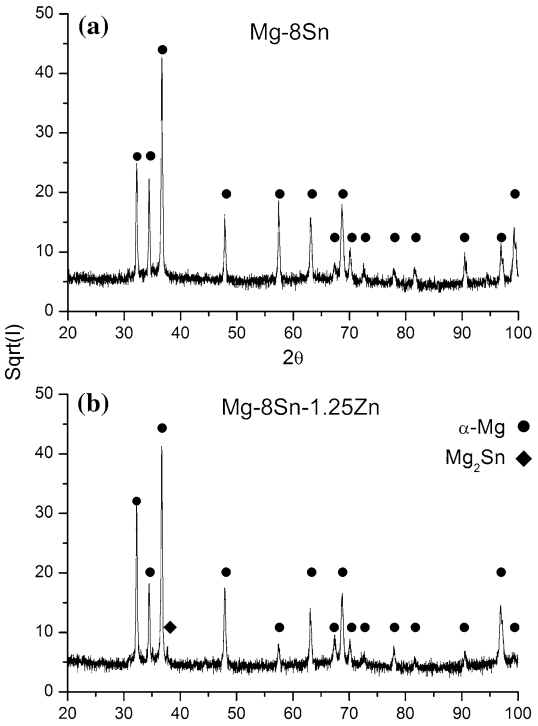

Fig. 9 XRD pattern recorded from **a** Mg–8Sn and **b** Mg–8Sn–1.25Zn after aging (175 °C, $t = 1.73 \times 10^5$ s, VMH-II)

Table 2 Phases detected by XRD in the Mg–8Sn and Mg–8Sn–1.25Zn alloys during aging at 175 °C

Aging time (s)	Mg–8Sn	Mg–8Sn–1.25Zn
$t = 0$ (solutionized state)	α-Mg	α-Mg
$t = 4.32 \times 10^4$	α-Mg	α-Mg
$t = 1.73 \times 10^5$	α-Mg	α-Mg, Mg_2Sn
$t = 2.76 \times 10^6$	α-Mg, Mg_2Sn	α-Mg, Mg_2Sn

after aging of the Mg–8Sn and Mg–8Sn–1.25Zn alloys. The increased Mg_2Sn amount was detected by XRD.

Figure 10 presents a SEM BSE micrograph of the (a) Mg–8Sn alloy, the (b) Mg–8Sn–1.25Zn alloy both in the as-quenched state, (c) Mg–8Sn alloy, and (d) Mg–8Sn–1.25Zn alloy both in the over-aged state (175 °C, $t = 2.76 \times 10^6$ s, VHM-III). As it can be seen (Fig. 10a, b), the solution treatment of the Mg–8Sn and the Mg–8Sn–1.25Zn alloy resulted in a homogenous microstructure. It appears that the solution treatment of the two alloys resulted in complete dissolution of all non-unary phases that were formed during casting. EDS analysis results of the Mg–8Sn and Mg–8Sn–1.25Zn alloys after the solution treatment are in good agreement with the designed composition and the composition that was measured by ICP-OE. EDS results did not detected any quartz tube (used during the solution treatment) related Si contamination in the Mg–8Sn or the Mg–8Sn–1.25Zn quenched alloys.

BSE micrographs of the aged (175 °C, $t = 2.76 \times 10^6$ s) Mg–8Sn and the Mg–8Sn–1.25Zn alloys (Fig. 10c, d, respectively) shows the formation of fine Mg_2Sn precipitates. The presence of Zn at the Mg–8Sn–1.25Zn alloy resulted in two significant effects: the number of the precipitates increases significantly, precipitates size decreases.

Discussion

CT-alloy composition and heat treatment selection

The increase in the Sn content results in a decrease in the α-Mg single-phase region (Fig. 1). The existence of a single-phase region is a prerequisite for effective solution treatment. The combined selection of: (i) the Sn and Zn content in the Mg–5.93Sn–3.01Zn alloy and (ii) the homogenization and solution treatment (505 °C for 48 h and 0.5 h at 525 °C, respectively) are not optimal [12]. The Mg–5.93Sn–3.01Zn alloy was heat treated in the liquid + α-Mg two phase region above the α-Mg single phase region (Fig. 5c; Table 1). This can result in a change in the microstructure as a result of the presence of the liquid phase and reduce the overall effectiveness of the solution treatment.

Two different solution treatments were optimized according to the equilibrium and non-equilibrium CT simulations while considering the difference in composition between the two alloys. The XRD and SEM results (Table 2; Fig. 10, respectively) for the solutionized Mg–8Sn and Mg–8Sn–1.25Zn alloys testified in the complete dissolution of the alloying elements in the α-Mg matrix. The information derived from the CT results allows the selection of an optimized alloy composition and the derivation of a composition-related solution treatment for the new alloys.

All the Mg–6.04Sn–*x*Zn alloys were heat-treated at 345 °C for 2 h to dissolve the low-temperature melting eutectic structures [12]. This was followed by heating (80 °C/h) and holding at 500 °C for 6 h [12]. The duration of the low- and high-temperature dwell at 345 and 500 °C appears to be too short for the complete dissolution of the eutectic structure and the homogenous distribution of Sn, which is the slow-diffusing element. As was mentioned before the alloy should be heat treated in a α-Mg single phase region.

The Mg–9.9Sn–*x*Zn alloys were homogenized at 505 °C for 48 h and then solution heat-treated for 0.5 h at 525 °C, followed by water quenching [13]. The heat treatment dwell time appears to be too short for an adequate solution

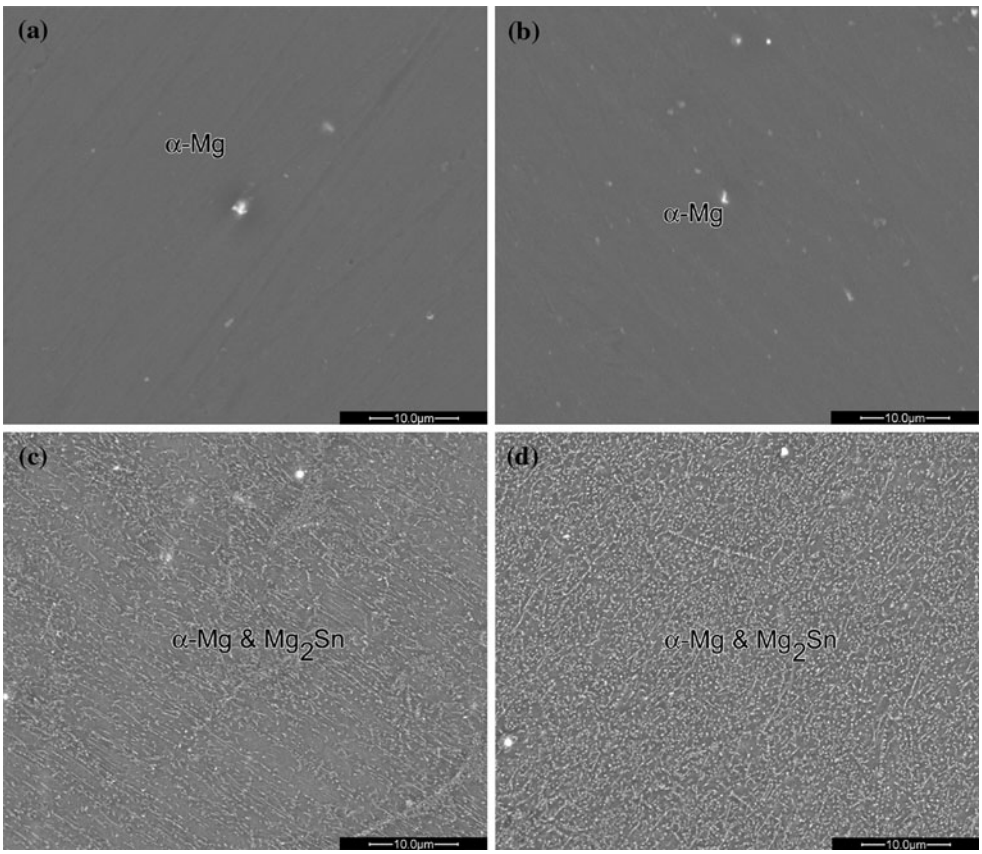

Fig. 10 SEM BSE micrograph of **a** Mg–8Sn alloy, **b** Mg–8Sn–1.25Zn alloy both in the as-quenched state, **c** Mg–8Sn alloy, and **d** Mg–8Sn–1.25Zn alloy both in the over-aged state (175 °C, $t = 2.76 \times 106$ s, VHM-III)

treatment. The lack of low-temperature dwell during the heat treatment of the Mg–9.82Sn–1.23Zn alloy may result in the melting of the eutectic structure during heating to the solution temperature. The thermal treatment applied can contribute to the inferior VMH response of the Mg–9.9Sn–*x*Zn alloys [13].

The composition selection for the Mg–3.8Sn–4.5Zn alloy was aimed at combined precipitation hardening via the formation of Mg–Zn ($MgZn_2$, MgZn) and Mg_2Sn precipitates [11, 14]. The Mg–3.8Sn–4.5Zn alloy was heat treated for 96 h at 300 °C, this was followed by quasi-static heating (1 °C/h) and a 96 h dwell at 465 °C [11]. The selected composition and the heat treatment applied [11] are aimed at the dissolution of the eutectic phase and a solution treatment in a α-Mg single phase region.

In the Mg–3.8Sn–4.5Zn [11], Mg–5.6Sn–4.41Zn–2.1Al [15], and Mg–3.98Sn–4.41Zn–0.62Y [16] alloys, the amount of Zn is higher or comparable to that of Sn. According to the CT simulation (see Fig. 7b), a significant amount of Mg-Zn precipitates is expected during aging. Since the diffusion of Sn in α-Mg is significantly lower than that of Zn [23], the Mg_2Sn precipitates will coarsen at a lower rate than the Mg–Zn precipitates. The Mg_2Sn precipitates are preferable in terms of temperature stability and hardening.

The aging temperature for the Mg–8Sn and Mg–8Sn–1.25Zn alloys was selected as 175 °C to prevent the possibility of any stable Mg–Zn ($MgZn_2$ or MgZn) precipitation in the Mg–8Sn–1.25Zn alloy (see Fig. 2b; Table 1). The Zn solute atoms are expected to be effective for manipulation of the Mg_2Sn precipitation in the α-Mg matrix, as expected Mg–Zn (MgZn and $MgZn_2$) precipitates were not detected in the Mg–8Sn–1.25Zn alloy.

The reliability of the Mg–Sn–Zn thermodynamic description appears to be high and can be further enhanced by addressing Sn solubility in the Mg-Zn intermetallics [17]. The application of the CALPHAD method for alloy design allows: CT analysis of published results, reduction of the resources needed for alloy design and increased precision during composition and thermal treatment selection.

The precipitation events in the high Sn content Mg–Sn and the Mg–Sn–Zn ternary system

In the Mg–8Sn and Mg–8Sn–1.25Zn alloys, the precipitation of Mg_2Sn is divided into two precipitation events (VMH-II and VMH-III peaks). The addition of Zn results

in the appearance of a VMH-I maximum, and increased VMH-II and VMH-III in the Mg–8Sn–1.25Zn alloy mentioned above.

The XRD results for the Mg–8Sn–1.25Zn alloy aged for 1.73×10^5 s (VMH-II) show that the formation of Mg_2Sn is enhanced in comparison with the Mg–8Sn alloy. The maximum VMH-III for the Mg–8Sn and Mg–8Sn–1.25Zn alloys aged for 2.76×10^6 s relates to the homogenous precipitation of Mg_2Sn in the α-Mg matrix [12, 13]. The addition of Zn refines the Mg_2Sn precipitates in the α-Mg matrix and hence increases VMH-III significantly.

A comparison between our results and those of Mendis et al. [12] shows that a major difference exists in the VMH measurement method used. The load used by Mendis et al. [12] was 10 kg, which seems too high for the detection of a fine matrix-related effect (Mg–Zn and Mg_2Sn precipitation). It should also be noted that only VMH-III was detected by Sasaki et al. [13] and Mendis et al. [12], this is attributed to overload during hardness measurements [12, 13]. The CT method used in the present work allows optimal composition selection and the derivation of a specific heat treatment that result in an optimal hardening response.

Figure 11 compares the VMH of the Mg–8Sn–1.25Zn alloy with that of the Mg–3.8Sn–4.5Zn [11], Mg–5.6Sn–4.41Zn–2.1Al [15], and Mg–3.98Sn–4.41Zn–0.62Y [16] alloys. As shown in the figure, the results are consistent with each other. Two VMH peaks, VMH-I and VMH-II, appear during aging after $\sim 1 \times 10^4$ and $\sim 1 \times 10^5$ s, respectively. TEM and XRD results correlated VMH-I with the presence of the Mg–Zn (MgZn or $MgZn_2$, which are expected to transform from the metastable Mg_4Zn_7 [10, 11]) phases, whereas VMH-II is related to the precipitation of the Mg_2Sn phase [11, 15, 16]. The experimental results

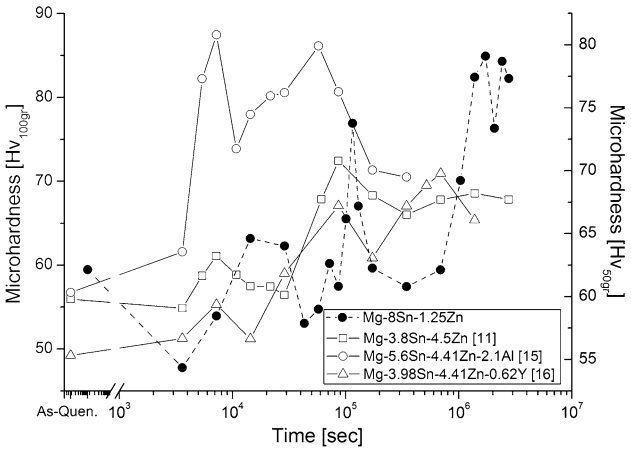

Fig. 11 Comparison of the VMH of the Mg–8Sn–1.25Zn, Mg–3.8Sn–4.5Zn [11], Mg–5.6Sn–4.41Zn–2.1Al [15], and Mg–3.98Sn–4.41Zn–0.62Y [16] alloys during aging

show that the Mg–Zn precipitates may serve as nucleation sites for Mg_2Sn precipitation [16, 27].

Table 3 presents the prominent features of the VMH results for the Mg–8Sn–*x*Zn, Mg–6.04Sn–*x*Zn [9], Mg–9.9Sn–*x*Zn [10], Mg–3.8Sn–4.5Zn [11], Mg–5.6Sn–4.41Zn–2.1Al [13], and Mg–3.98Sn–4.41Zn–0.62Y [14] alloys. The hardening effect of Mg_2Sn precipitation in all alloys is clearly evident in the formation of VMH-III. The increase in the Sn content reduces the time it takes to reach maximum peak hardness. For all ternary alloys the increase in Zn content increases VMH-III by 15 to 45%. The increase in the Zn content of Mg–6.04Sn–*x*Zn and Mg–9.88Sn–*x*Zn [12, 13] tends to decrease the time needed to reach VMH-III; in our results for Mg–8Sn–*x*Zn, the time it takes to reach VMH-III is roughly unaffected by the 1.25 wt% Zn additions.

Table 3 The VMH-x [HV] of the peak x (I, II, III) and the time it takes to reach VMH peak ($t_{VMH\text{-}x}$, (s)) for the Mg–8Sn–*x*Zn, Mg–6.04Sn–*x*Zn [12], Mg–9.9Sn–*x*Zn [13], Mg–3.8Sn–4.5Zn [11], Mg–5.6Sn–4.41Zn–2.1Al [15], and Mg–3.98Sn–4.41Zn–0.62Y [16] alloys

	VMH-I	$t_{VMH\text{-}I}$	VMH-II	$t_{VMH\text{-}II}$	VMH-III	$t_{VMH\text{-}III}$
Mg–6.04Sn [12]	–	–	–	–	48.6	$\sim 7.57 \times 10^6$
Mg–6Sn–1Zn [12]	–	–	–	–	56.76	$\sim 8.20 \times 10^6$
Mg–5.93Sn–3.01Zn [12]	–	–	–	–	70.28	$\sim 8.02 \times 10^5$
Mg–8Sn	–	–	65.4	$\sim 1.0 \times 10^5$	69	$\sim 2.07 \times 10^6$
Mg–8Sn–1.25Zn	64.6	$\sim 1.44 \times 10^4$	73.76	$\sim 1.15 \times 10^5$	79	$\sim 2.07 \times 10^6$
Mg–9.9Sn [13]	–	–	–	–	62	$\sim 1.39 \times 10^6$
Mg–9.88Sn–0.25Zn [13]	–	–	–	–	71.2	$\sim 4.59 \times 10^5$
Mg–9.82Sn–1.23Zn [13]	–	–	–	–	78.7	$\sim 4.7 \times 10^5$
Mg–3.8Sn–4.5Zn [11]	78.7	$\sim 7.2 \times 10^3$	72.4	$\sim 8.64 \times 10^4$	–	–
Mg–5.6Sn–4.41Zn–2.1Al [15]	87.45	$\sim 7.2 \times 10^3$	86.13	$\sim 5.76 \times 10^4$	–	–
Mg–3.98Sn–4.41Zn–0.62Y [16]	55.31	$\sim 7.2 \times 10^3$	67.0	$\sim 8.64 \times 10^4$	–	–

The influence of Zn on precipitation hardening in Mg–Sn–Zn alloys

A detailed analysis of alloys Mg–3.8Sn–4.5Zn [11], Mg–5.6Sn–4.41Zn–2.1Al [13], and Mg–3.98Sn–4.41Zn–0.62Y [14] at short aging times ($t < 3 \times 10^5$ s) reveals the presence of VMH-I ($t = 7.2 \times 10^3$ s) and VMH-II ($t = 8 \times 10^4$ s). The required time for the two VMH peaks in alloy Mg–8Sn–1.25Zn appears to be longer, which is attributed to the reduced Zn amount in the Mg–8Sn–1.25Zn alloy.

VMH-I is related to the formation of Mg–Zn precipitates. Controlled decomposition of the Mg–Zn solid solution results in an age-hardening effect: Mg_4Zn_7 was detected as the metastable phase, $MgZn_2$ as the intermediate phase [10, 11].

The presence of VMH-II in the Mg–8Sn sample proves that the Mg_2Sn precipitation at this stage is not directly connected to a Zn-related effect. VMH-II can be related to the heterogeneous nucleation of Mg_2Sn on microstructural features (dislocations, grain boundaries, etc.). The presence of Zn increases the hardening response by the increased nucleation and refinement of the Mg_2Sn precipitates. The Mg–Zn precipitates may serve as additional sites for Mg_2Sn nucleation [26], thus increasing the VMH-II peak. It is not yet clear what kind of Mg–Zn phases serve as preferred nucleation sites for Mg_2Sn (Mg_4Zn_7 or $MgZn_2$).

The VMH-III maximum relates to the homogenous precipitation of Mg_2Sn in the α-Mg matrix [12, 13]. The addition of Zn increases the VMH-III peak. This can be realized in several ways. The presence of Zn reduces the stacking fault energy and substantially increases the number of stacking faults in α-Mg. The stacking fault planes may serve as preferential places for Mg_2Sn nucleation, thereby increasing the number of nucleation sites significantly. It was also assumed [12, 13] that the preferred segregation of Zn on specific planes of Mg_2Sn in α-Mg may reduce the interfacial energies and thus reduce the driving force for coarsening. Additional nucleation sites for Mg_2Sn may be the Zn-vacancy or Sn–Zn-vacancy clusters that can possibly form in the Mg–Sn–Zn alloys. By this means, the addition of Zn refines the Mg_2Sn precipitates in the α-Mg matrix and hence increases VMH-III significantly.

Conclusions

The optimization of Mg–Sn–Zn alloys composition and heat treatment design was performed utilizing the CALPHAD method. The composition of the ternary alloy was set as Mg–8Sn–1.25Zn. The Sn and Zn content was designed and confirmed to be within the α-Mg solubility limit at the solution treatment temperature. The addition of Zn and the heat treatment applied resulted in the enhancement and refinement of the Mg_2Sn precipitation. Three VMH maxima were detected and attributed to the precipitation of metastable Mg-Zn phases precipitates, the heterogeneous precipitation of Mg_2Sn on microstructural features, and homogenous Mg_2Sn precipitation in the α-Mg matrix. Several Mg–Sn–Zn alloys were evaluated by CT simulations, and their hardening response was analyzed. The CT simulations were found to be consistent with the experimental results.

Acknowledgements Y. Shahaf, T. Leviatan, and Y. Maoz are acknowledged for their help in the sample preparation and measurements. J. Wang is acknowledged for sharing the Mg-Sn-Zn Thermo-Calc database. This study was partially supported by the Bernstein Research Fund, the authors acknowledge the fund for its support.

References

1. Pekguleryuz MO, Kaya AA (2003) Adv Eng Mater 5:866
2. Wendt A, Weiss K, Ben-Dov A, Bamberger M, Bronfin B (2005) Magn Technol 2005:269
3. Smithells CJ, Brandes EA, Brook GB (1998) Smithells light metals handbook. Butterworth-Heinemann, Oxford
4. Hort N, Huang Y, Kainer UK (2006) Adv Eng Mater 8:235
5. Saunders N, Miodownik AP (1998) Calphad: a comprehensive guide. Pergamon, Oxford
6. Bamberger M (2006) J Mater Sci 41:2821. doi:10.1007/s10853-006-6294-4
7. Schmid-Fetzer R, Grobner J (2001) Adv Eng Mater 3:947
8. Alloy Phase Diagrams (2010) ASM International, http://products.asminternational.org/hbk/index.jsp. Accessed 1 Sept 2010
9. Avedesian MM, Baker H (1999) Magnesium and magnesium alloys. ASM International, Materials Park, OH
10. Gao X, Nie JF (2007) Scr Mater 56:645
11. Cohen S, Goren-Muginstein G, Avraham S, Bamberger M, Rashkova B, Dehm G (2005) Z Metallkd 96:1081
12. Mendis CL, Bettles CJ, Gibson MA, Hutchinson CR (2006) Mater Sci Eng A 163:435
13. Sasaki TT, Oh-ishi K, Ohkubo T, Hono K (2006) Scr Mater 55:251
14. Rashkova B, Prantl W, Görgl R, Keckes J, Cohen S, Bamberger M, Dehm G (2008) Mater Sci Eng A 494:158
15. Harosh S, Miller L, Levi G, Bamberger M (2007) J Mater Sci 42:9983. doi:10.1007/s10853-007-2059-y
16. Gorny A, Bamberger M, Katsman A (2007) J Mater Sci 42:10014. doi:10.1007/s10853-007-1998-7
17. Meng F, Wang J, Liu L, Jin Z (2010) J Alloys Compd 508:570
18. Sundman B, Jansson B, Andersson JO (1985) Calphad 9:153
19. Thermo-Calc AB, http://www.thermocalc.com/ Stockholm
20. Reed-Hill RE, Abbaschian R (1992) Physical metallurgy principles. PWS-Kent Publishing Company, Boston
21. Scheil E (1942) Z Metallkd 34:70
22. Gulliver GH (1913) J Inst Met 9:120
23. Ed. Mehrer H (1990) Diffusion in solid metals and alloys. Landolt-Börnstein numerical data and functional relationships in science and technology. Springer-Verlag, Berlin
24. Setaram Instrumentation, http://www.setaram.com/ Caluire
25. The International Centre for Diffraction Data, http://www.icdd.com/ Newtown Square
26. http://www.fei.com/ Eindhoven
27. Gorny A, Katsman A (2008) J Mater Res 23:1228